Mechanical effects of fatigue and charge on CMOS MEMS

Kevin M. Frederick[*] and Gary K. Fedder[*+]
[*]Department of Electrical and Computer Engineering and [+]The Robotics Institute
Carnegie Mellon University, Pittsburgh, PA 15213-3890

ABSTRACT

CMOS MEMS devices, fabricated from up to 13 layers of materials to create independent conducting paths, are subject to incremental fracture at high stress and to charging effects. This paper expands on preliminary research, which has revealed several stages of change in CMOS MEMS physical properties as they are exposed to resonant motion. Cracks are first induced inside the stiffest layers, often silicon dioxide, in laterally resonant test structures with cyclic stress of 620 MPa. Prior to cracking, the aluminum top layer of the structure can also deform, which affects the electrical integrity of the conductor. Measured frequency responses of folded-flexure resonators demonstrate a nonlinear Duffing effect, producing a mushroom-shaped resonant peak. Cyclic stress of 70 MPa at the maximal stress points was insufficient to induce significant mechanical fracture in folded flexure resonators after 5 billion cycles, however an onset of change in stiffness was detected. Devices with a fixed dc actuation voltage experienced a change in the electrostatic force attributed to charge accumulation in polymer and oxide layers. The force decayed with an approximate one-hour time constant while resonant frequency and quality factor remained constant.

Keywords: fatigue, charging, CMOS MEMS

1. INTRODUCTION

Microelectromechanical systems (MEMS) that are manufactured from the interconnect layers available for Complimentary Metal Oxide Semiconductor (CMOS) integrated circuits have unique failure modes[1,2,3]. In CMOS micromachining, an anisotropic reactive ion etch is performed through oxide layers that are not protected by a top metal layer until the silicon substrate is exposed. A timed isotropic etch then removes the exposed silicon while leaving the oxide and metal layers intact. Sufficiently thin microstructures are completely undercut and free to move as shown in the cross section of Figure 1. The CMOS-MEMS devices have multiple oxide, TiW, and aluminum layers within each beam as shown in Figure 2.

The various materials that make up a CMOS MEMS device have different properties and thus contribute different amounts of stiffness and strength to any given beam. These internal differences lead to a failure sequence as some of the internal layers will fracture before others. To explore these effects, a test setup that automatically actuates any MEMS device at its resonant frequency over an extended period of time has been developed. The device is characterized periodically to establish its current resonant frequency and quality factor. The amplitude of a device's lateral motion is detected electronically and recorded at each characterization stage as well, to provide an indication of the device stiffness. The automation facilitates very long term testing without manual interaction, and can be used to determine the multiple stages of failure inherent to CMOS MEMS devices.

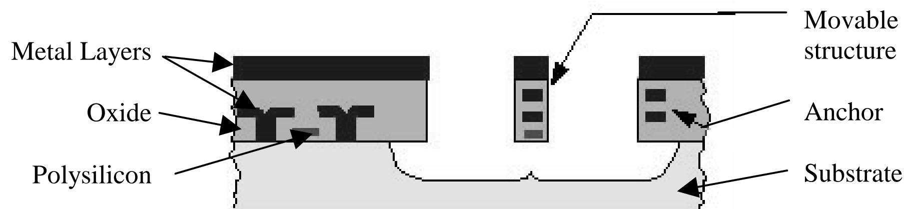

Figure 1. Cross section of CMOS-MEMS process after release etch.

Correspondence: Email kevinf@cmu.edu, WWW: http://www.ece.cmu.edu/~mems; Tel: (412) 268-4594; Fax: (412) 268-4595

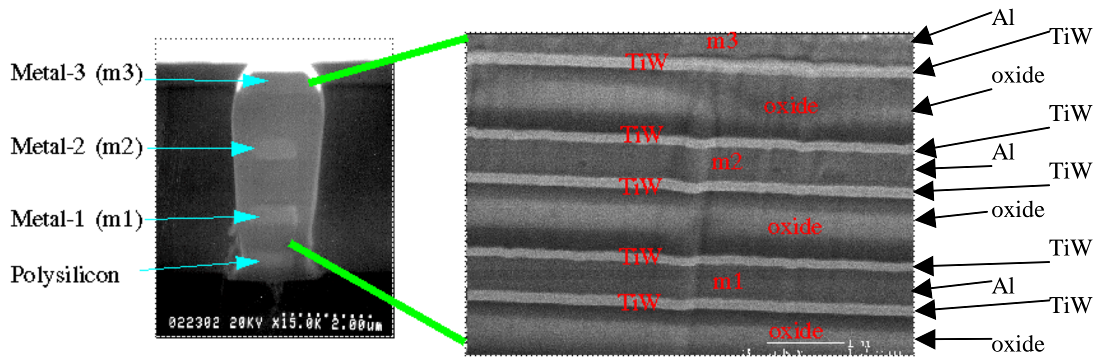

Figure 2. SEM of a beam cross section, showing detailed layers.

Understanding and characterizing the cracking phenomenon has critical importance for CMOS MEMS because the mechanical and electrical integrity of the device must be maintained. Ideally this breakdown can be avoided by operating below the threshold that causes fracture. It is believed that this threshold can be determined using extrapolated data for a given beam configuration with a known set of included layers. As the displacement of the chip is reduced to a level comparable to its expected application, the number of cycles necessary for fracture increases. By extrapolating the trend of actuation distance vs. cycles to failure, a threshold for safe operation may be determined.

2. BACKGROUND

Prior characterization experiments on CMOS MEMS clearly indicated that several stages of failure are present in CMOS MEMS. Figure 3 shows prior results from resonating a CMOS-MEMS fan structure with a constant lateral free-end deflection of 2 μm. A notch is fabricated at the intended center of rotation to focus the stress induced by motion and accelerate fatigue within the device. The cyclic maximum stress at the notch is 124 MPa. The notch section included all 13 layers that are present in the CMOS MEMS beam. The sequential drop in resonant frequency is a result of annealing, cracking, or deformation present within one or more of the layers on the CMOS MEMS beam structure. The initial SEM taken of a tested device, as seen in Figure 4, confirmed this hypothesis. There was also clear evidence that a threshold existed for device displacement during actuation that would cause it to catastrophically fail and actually break off from its anchor. The plot in Figure 3 demonstrates a case where the stress from displacement was insufficient to cause catastrophic failure. However, when the displacement was increased five-fold to 10 μm (620 MPa stress), the device did fracture at the notch after 50 million cycles.

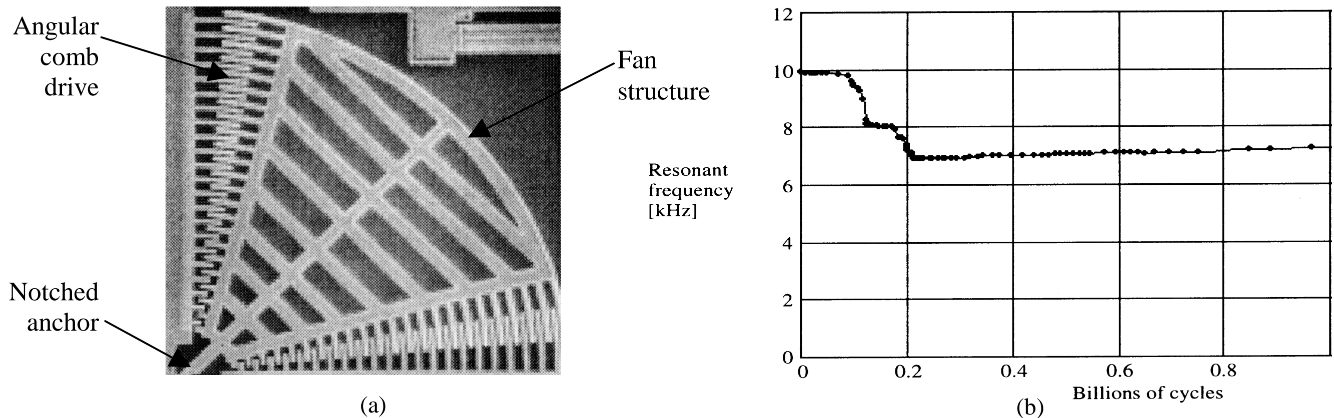

Figure 3. Prior durability testing. (a) Fan test structure. (b) Resonant frequency change with time[4].

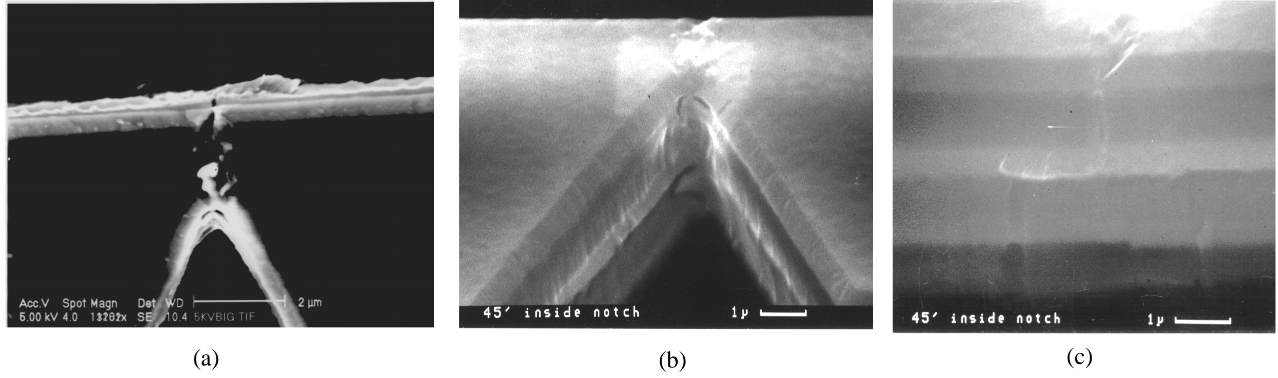

(a) (b) (c)

Figure 4. Fan structure after cyclic stress, showing a (a) top view, (b) side view inside the notch, (c) backside of the notch.

3. RESONANT DEVICE DESCRIPTION

The resonator is a micromechanical spring-mass system embodied as a central shuttle plate suspended by two folded-flexure springs, as shown in Figure 5. Electrical signals are connected to the resonator with probes placed on large pads. The force-displacement relation usually has a underdamped characteristic with a well-defined resonant peak. The spring constant is dominated by the bending of the slender long beams in the flexure. These beams have an effective Young's modulus E, beam bending moment of inertia I, beam length L and beam width w. The spring force, F_k, and moment, M, acting on the shuttle are

$$F_k = \frac{6EI}{L^3} x \tag{1}$$

$$M = \frac{F_k L}{2} = \frac{3EI}{L^2} x \tag{2}$$

where x is the shuttle lateral displacement. Maximum stress, σ_{max}, occurs at the base of the flexure beams and is given by

$$\sigma_{max} = \frac{Mw}{2I} = \frac{3}{2} E \frac{wx}{L^2} \tag{3}$$

Interdigitated comb-finger electrostatic actuators (called comb drives) are attached to the left and right sides of the shuttle. The comb drive capacitance is linear with displacement and is given by

$$C = C_o x \tag{4}$$

where C_o is in units of F/m. When a voltage, V, is applied to one of the comb drives, the resulting attractive electrostatic force,

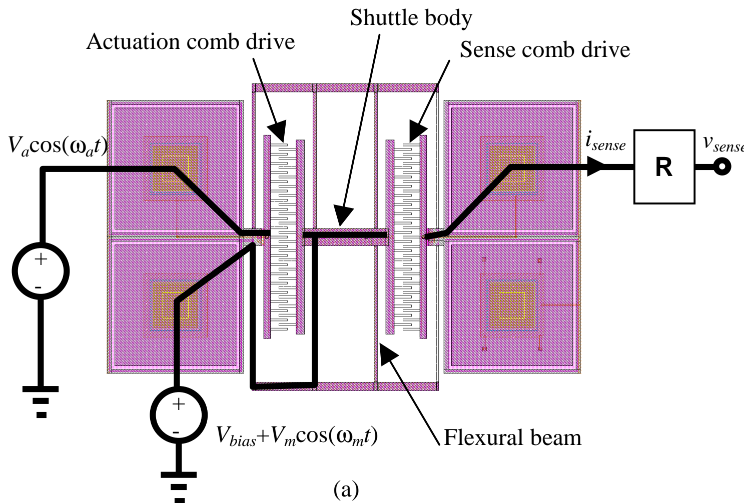

(a)

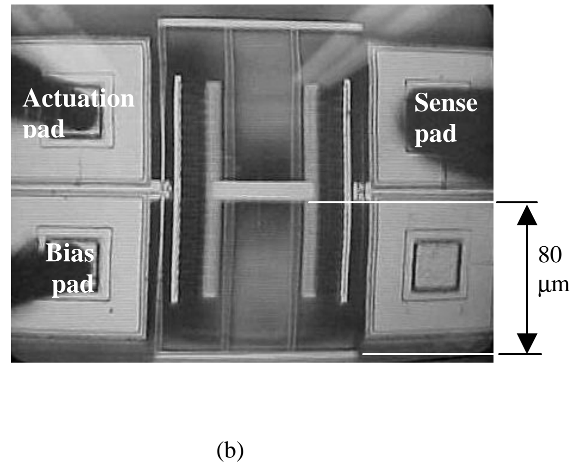

(b)

Figure 5. Folded-flexure resonator with 80 µm flexural beam length. (a) Layout. (b) Structure driven at resonance.

$$F_e = \frac{C_o V^2}{2} \tag{5}$$

is proportional to the applied voltage squared, and is independent of displacement.

The resonator is connected as shown in the schematic in Figure 5. An actuation signal, $V_a \cos(\omega_a t)$, is applied to the stator of the left-hand comb drive. The shuttle is connected to a dc bias voltage, V_{bias}, in series with a sinusoidal modulation voltage, $V_m \cos(\omega_m t)$. The stator of the right-hand comb drive is connected to a transresistance amplifier with a gain of R = 1MV/A. The op-amp feedback keeps the voltage on the right-hand stator fixed at 0 V. From (5), the total electrostatic force acting on the resonator shuttle is

$$F_{total} = C_o V_a \left[-\frac{V_a}{4} + V_{bias}\cos(\omega_a t) - \frac{V_a}{4}\cos(2\omega_a t) + V_m \cos(\omega_m t)\cos(\omega_a t) \right] \tag{6}$$

The first term in (6) is a dc offset force, the second term is at the fundamental drive frequency, the third term is at twice the fundamental drive frequency, and the fourth term is at $\omega_m \pm \omega_a$. If $V_a << 4V_{bias}$, then the fundamental drive term dominates.
The output voltage of the transresistance amplifier is

$$V_{out} = -R\frac{d\left[CV_{bias} + CV_m\cos(\omega_m t)\right]}{dt} = -RC_o\left[V_{bias} + V_m\cos(\omega_m t)\right]\frac{dx}{dt} + RC_o V_m \omega_m \sin(\omega_m t)x \tag{7}$$

The second term in (7) dominates if the resonator is being excited primarily by the fundamental drive term (*i.e.*, $x \approx x_o\cos(\omega_a + \phi)$) and $\omega_m >> \omega_a$. The modulation voltage shifts the displacement signal out to the frequency band around ω_m. For steady-state sinusoidal displacement, the relative displacement amplitude is detected by measuring the spectrum of the output voltage at $\omega_m \pm \omega_a$.

4. EXPERIMENTAL TEST SETUP

Automated test setups for MEMS characterization have been reported by Exponent[5], MIT[6] and AFRL[7]. The test setup in the present work uses electrical sensing to monitor resonance frequency, resonant amplitude and damping factor. The testbed controller is implemented LabVIEW [8], with instruments controlled over the General Purpose Interface Bus (GPIB).

The physical configuration of the test setup is shown in Figure 6. The HP33120A function generator at the top left in Figure 6 provides the sinusoidal actuation signal. The shuttle body is connected to a DC bias in series with a second function generator that supplies the modulation voltage. Parasitic capacitance between connections to the actuator comb drive and the sense comb drive causes feedthrough to the output with a frequency component at ω_a. Similar parasitic capacitance between the shuttle and output comb-drive connections causes feedthrough at ω_m. To minimize parasitic capacitance on the sense comb drive, the transresistance amplifier was constructed directly on the probe needle. The HP 4395A spectrum analyzer is used to resolve the mechanical displacement signal at $\omega_m \pm \omega_a$, and to determine the relative displacement magnitude. An output spectrum illustrating these effects is shown in Figure 6. The components at $\omega_m + \omega_a$ and $\omega_m - \omega_a$ are not equal because of a time-invariant frequency dependence in the readout electronics. The averaging capabilities of the spectrum analyzer generate consistent measurements although the extra detection time necessary sacrifices the ability to detect extremely fast changes in device characteristics.

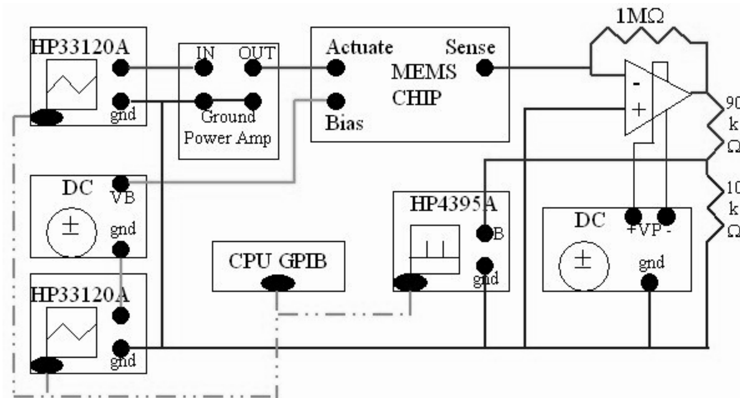

Figure 6. Schematic of the automated test setup.

5. MEASUREMENT ALGORITHM

By controlling the actuation of the device with a computer, reliable and continuous measurements of the resonant frequency and the resonant peak width can be accomplished with 10 Hz resolution. The diagram in Figure 8 shows the general flow of control that the computer executes through its automated testing of a device.

The flow is designed to work on a device for which the initial resonant frequency is already known with some accuracy. The course initial sweep will activate the device with a range of frequencies around a set starting point. If the resonant frequency is not known prior to experimentation, the separation between each tested frequency or the number of tested frequencies can be increased. As the number of tested frequencies is increased, the initial sweep does take more time. Unfortunately, some CMOS MEMS devices have a small but rapid initial change in resonant frequency. This change is only captured by the test setup when the change occurs after the initial sweep. A constant amplitude of actuation voltage is used throughout the testing so highly accelerated testing, which is accomplished using an extremely high input signal magnitude, will not detect changes which occur during the initial coarse frequency sweep.

The use of a constant actuation amplitude also allows the study of the motion magnitude induced at resonance. As the device begins to crack or change its physical properties during extended actuation, the stiffness of the device is likely to be reduced. Thus an increase in the amplitude of the sensing output signal is expected while the resonant frequency drops. Careful tracking of the amplitude of the output signal along with an associated change in resonant frequency can determine which structural layers within a CMOS MEMS chip are cracking as a device is actuated over an extended period of time.

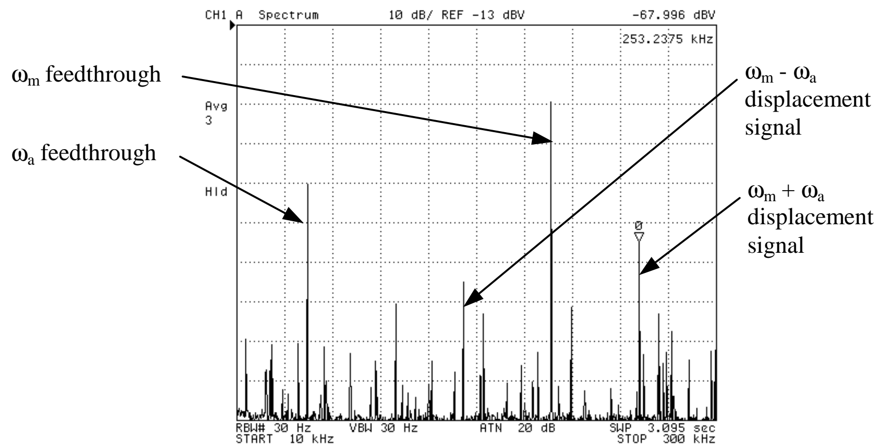

Figure 7. A typical output voltage spectrum during resonant operation (53kHz actuation, 200kHz carrier).

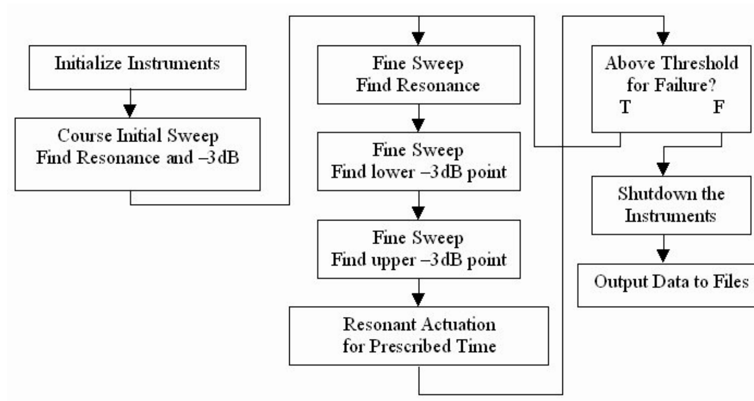

Figure 8. Frequency sweep algorithm.

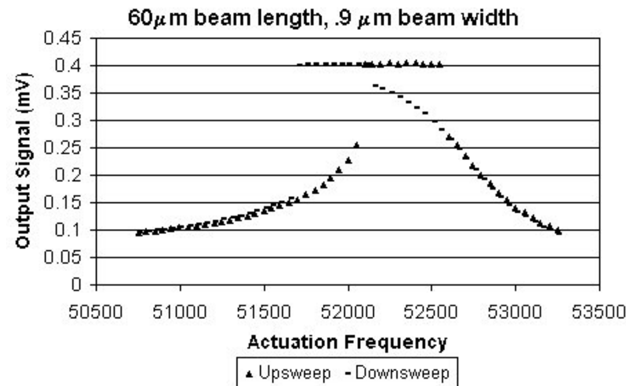

Figure 9. Frequency response of a resonator exhibiting the nonlinear Duffing effect.

The frequencies where the output response is 3 dB below the resonant frequency is determined by performing two sweeps of varying actuation frequency above and below the resonant frequency. The center of the sweep is set to the -3 dB frequency found during either the initial course frequency sweep or from a previous fine sweep when available from an extended test. The first encounter of -3dB magnitude is determined to be the -3 dB frequency for the current sample point. As verification of proper operation, the setup accurately characterizes an analog first-order bandpass filter with a variable gain and width of its peak response. The algorithm was able to successfully determine the resonant frequency and the -3 dB points. Quality factor is then calculated as the resonant frequency divided by the peak's bandwidth.

The micromechanical resonators tested have a high quality factor of around 100. Furthermore, the resonators display a distortion in the frequency response arising from a nonlinear spring constant (called the Duffing effect), usually caused by axial tension or compression in the flexure beams. This effect is accentuated when a device is driven with a large actuation amplitude. The frequency response of a resonator with 60 µm long beams is shown in Figure 9 to illustrate this effect. The simple -3 dB algorithm encounters a problem when the frequency response has discontinuities arising from the Duffing effect. Currently, only an increasing frequency sweep is used to search for the resonant peak during extended testing, so resonant peaks that bend over to the lower frequencies will not be accurately characterized. Occasionally, the -3 dB frequency changes is detected on the wrong side of the resonant peak, producing inaccurate results as the -3 dB frequencies would be identical. This crossover problem is remedied by shifting the -3dB sweep further away from the peak, far enough to ensure that the sweep will only include frequencies on the intended side of the resonant peak. The -3 dB frequencies could be measured more directly by performing both increasing and decreasing frequency sweeps during extended testing but this was not implemented in the present setup.

The final step in testing the MEMS device is actuating the device consistently at its resonance over an extended period of time beyond the characterization sweeps. However, the device characteristics may change quickly as it is first actuated. The time between characterization measurements can be adjusted as the device continues through its testing to ensure that the drive frequency is set accurately to the device resonance. The period between characterization measurements can be increased to reduce unnecessary interruptions in the stimulus while searching for long-term failure modes.

The measurements may be stopped based upon a change in resonant frequency, so the device can be removed for examination. For example, the device's internal structure may have changed if the resonant frequency drops below a certain value. Alternatively, the user can simply tell the computer to finish its current characterization run and then shut down the instruments. When an experimentation run is terminated, data is exported to files including the time that each extended resonance session began, and the sampled data of resonant frequency, resonant amplitude, and quality factor. If another set of characterization and cyclic stress actuation is desired, then the last resonant frequency and the -3 dB frequencies are stored by the program and used as base values for the next characterization sequence. The computer simply uses these values as the initial center of its sweeps to determine the resonant frequency and quality factor. The condition of each resonator must be recorded so that the number of mechanical cycles and stress the device has experienced during testing may be related directly to its total lifetime.

6. EXPERIMENTAL RESULTS

Absolute values of displacement were determined by taking optical measurements of vibrational envelopes of wide parts of the shuttle body structure. To begin the testing of a new device, it was necessary to determine its approximate resonant frequency. Each new folded-flexure device was initially actuated manually with a minimal actuation voltage of 2 to 3 V peak-to-peak, which excited motion within the optical resolution of the microscope. Care was taken to quickly find the smallest indication of motion amongst an expected frequency range of 10 kHz to 100 kHz. Once the resonant frequency was found, the amplitude of the actuation signal was reduced and the frequency was moved away from the resonant peak. Then, the computer automated test setup assumed the responsibility of actuating the device and recording its response to facilitate tracking over time.

The initial coarse frequency sweep, which more accurately determines the resonant frequency and peak width, is not recorded. The device is typically only in resonance for a small period of this testing since the frequency steps involved in the sweep are relatively large. If the step size was minimized, as if a device was beginning continued testing after some external examination, its effect on the changes of the resonant frequency and other characteristics would have to be considered.

Results of resonant frequency, resonant amplitude, and quality factor for three different resonator geometries are given in Figures 10-12. Each resonator has 60 μm-long flexural beams, but varying beam widths and shuttle masses. For this study, the primary value of interest is the maximum stress at the base of the beams. The maximum stress was 55, 61, and 70 MPa, respectively, for data in Figures 10-12. Resonators in Figures 10 and 11 had slender 0.9 μm-wide beams, however the shuttle mass is larger for the device in Figure 11. The difference in mass gives rise to a 10 kHz difference between the resonant frequencies. The resonator in Figure 12 had wider 1.7 μm beams in its suspension.

The characterization algorithm occasionally failed because of the Duffing effect, giving rise to a significant shift in the plotted sense amplitude and frequency. This data measurement error is especially apparent in the frequency response of the resonator in Figure 10, which had a large Duffing effect. Because these outlying points are artifacts of the measurement algorithm, they are ignored in the discussion.

The resonant frequency of the devices subjected to 55 MPa and 61MPa cyclic stress changed less than 0.1% given the 50 Hz step resolution of these two experiments. The device with maximum stress of 70 MPa exhibited a decrease in resonant frequency starting at around 3.7 billion cycles (10.3 hr), implying that the mechanical integrity of the resonator was impacted, but entire fracture through layers had not occurred. In all cases, the quality factor remained constant (the variation in quality factor in Figure 10 is an artifact of the measurement technique). The constant quality factor is not surprising, since air damping is the dominant dissipative mechanism. The combination of current and prior measurements place a bound on internal fracture at between 70 MPa to 124 MPa.

A transient increase in resonant amplitude is present in each test of the resonators. The resonator subjected to 61 MPa of maximum stress had the greatest increase equal to 5.5% of the sense voltage. If mechanical annealing or cracking had taken place, the stiffness of the springs would have changed and altered the resonant frequency of the device. Therefore, it is not believed that mechanical processes, such as spring softening, were responsible for the shift in signal amplitude. The increase in output displacement amplitude indicates an increase in the amplitude of electrostatic force applied to the device.

To investigate charging effects, some initial screening experiments were performed. Two folded-flexure resonators with 150 μm-long beams were subjected to a dc force source intended to pull the shuttle body toward one side. A 10 V dc signal was applied to one device and a 10 V amplitude 10 Hz square wave was applied to the other device. The results in Figure 13 show the relative change in output sense voltage. The dc-driven output signal was around 0 V after the dc source was activated but then rapidly dropped 0.15mV after 160 s. A wait of approximately 50 min (600 samples) was necessary before the device output amplitude was fully stabilized. The square-wave driven device showed a smoother transition but its output also stabilized after 1 hr 20 min of testing. The slow time constant on the order of 1 hour is consistent with the transient amplitude plot shown in Figure 11.

Mobile charge at the air-electrode interface and in the surrounding dielectrics of the comb drive may be responsible for the transient in output sense voltage. The dielectrics include both the oxide layers surrounding the beam metallization and a thin layer of polymer that remains on the sidewalls of the devices after they are etched for release. The charge migrates slowly (with time constant of 1 hr) to or from the polymer and/or oxide layers. The charge migration induced by the input dc voltage

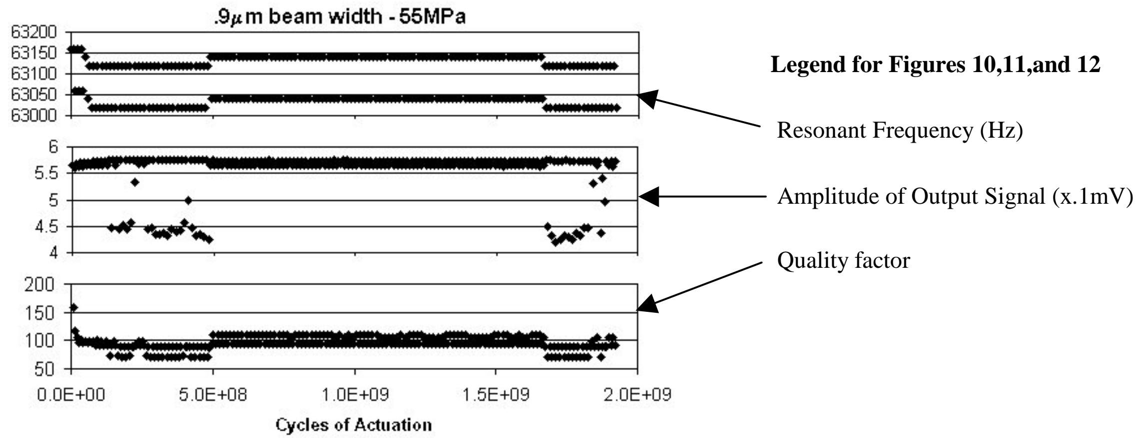

Figure 10. Extended test of a resonator with 60 μm-long, 0.9 μm-wide beams at 55 MPa maximum stress. The outlying points in amplitude is from a failure of the measurement algorithm in the presence of a strong Duffing effect.

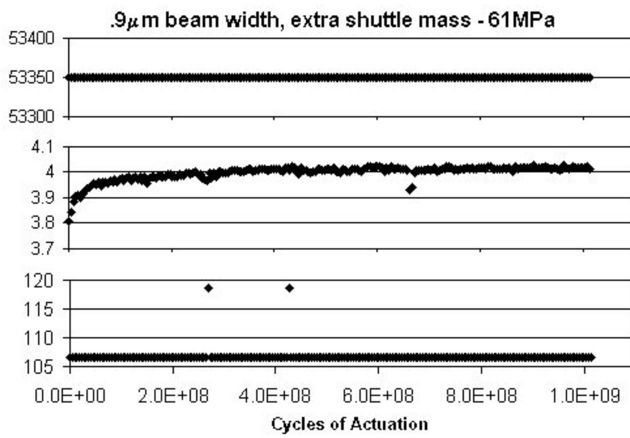

Figure 11. Extended test of a resonator with 60 μm-long, 0.9 μm-wide beams at 61 MPa maximum stress. Axes are defined on Figure 10.

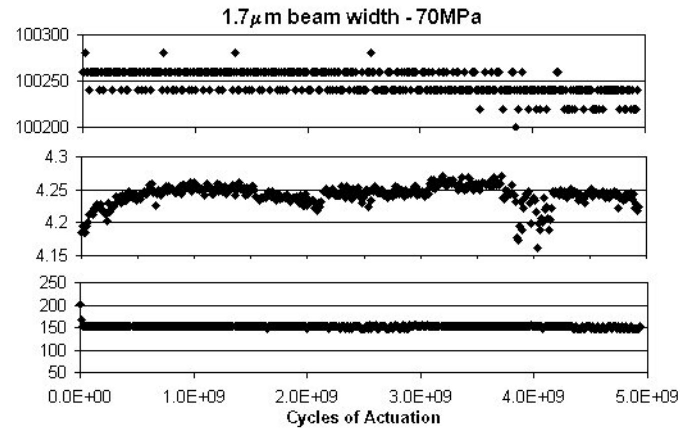

Figure 12. Extended test of a resonator with 60 μm-long, 1.7μm-wide beams at 70 MPa maximum stress. Axes are defined on Figure 10.

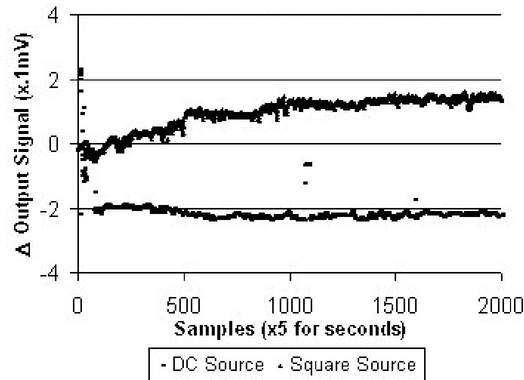

Figure 13. Relative sense output of dc-actuated folded-flexure resonators. Bottom trace is the relative output signal with a dc voltage applied, and the top trace is with a square-wave voltage applied.

decreases the effective gap in the comb drive and increases the electrostatic force. Since the mobile charge moves very slowly, it does not contribute significantly to displacement current. However, the change in force shifts the shuttle body towards the actuation comb drive, which reduces the capacitance between the shuttle body and the sense fingers and reduces the output sense signal. The device subjected to the square-wave input signal exhibits an increasing effective gap in the actuation comb drive, which increases the output signal magnitude. This effect is believed due to relaxation of trapped charge moving out of the polymer and oxide layers.

7. CONCLUSION

Two important issues for CMOS microstructures are the constancy of material properties when subjected to stress, and the charge relaxation in surrounding dielectric layers. The folded-flexure structures used for testing did not exhibit significant cracking or mechanical failure at 61 MPa of cyclic induced stress at the maximum stress points. At these relatively low stress levels, the resonant frequency did not change within the accuracy of the measurement system. An onset of cracking appeared at 70 MPa of stress. However, 70 MPa was the limit of the devices tested, and future work should include testing of similar resonant devices designed for stress concentrations in the range of 70 MPa to 124 MPa.

A significant Duffing effect in the resonant motion of folded flexure devices was present despite the use of folded flexures intended to minimize the effect. The resonant peak formed a mushroom shape when the amplitude of motion and detection jumped as the frequency was being swept either up or down. It is possible to further develop the measurement setup to robustly characterize structures with this effect.

Electrostatic force on the structures experienced an initial transient change with a time constant of about 1 hour. The change in force is believed to arise from mobile charge in surrounding oxide and in polymer residues remaining on the sidewalls from the etching process. Further study is required to understand the exact nature and location of the charging.

8. ACKNOWLEDGEMENT

The authors would like to thank Xu Zhu and Micheal S.-C. Lu for their help in understanding expected fracture modes and device characteristics. Dr. John Neumann was also helpful in learning the programming environment in LabVIEW through tutorial examples of his previous work. This research effort is sponsored by DARPA and U.S. AFRL, under agreement number F30602-97-2-0323.

9. REFERENCES

1. G. K. Fedder, S. Santhanam, M. L. Reed, S. C. Eagle, D. F. Guillou, M. S.-C. Lu, and L. R. Carley, “Laminated High-Aspect-Ratio Microstructures In A Conventional CMOS Process,” *Sensors & Actuators A*, vol. A57, no. 2, pp. 103-110, March 1997.
2. M. S.-C. Lu, X. Zhu and G. K. Fedder, “Mechanical Property Measurement of .5µm COMS Microstructures,” in *Proc. MRS 1998 Spring Meeting, Symposium N, San Francisco, CA, April 13-17, 1998*.
3. X. Zhu, D. W. Greve, R. Lawton, N. Presser, and G. K. Fedder, “Factorial Experiment on CMOS MEMS RIE Post Processing,” in *Proc. of the 194th Electrochemical Society Meeting, Symposium on Microstructures and Microfabricated Systems IV,* vol. 98-14, Boston, MA, Nov 1-6, 1998, pp. 33-42.
4. G. K. Fedder and R. D. Blanton, “Characterization and Reliability of CMOS Microstructures,” in *Proc. of SPIE Symposium on Micromachining and Microfabrication, Conf. on MEMS Reliability for Critical and Space Applications,* vol. 3880, Santa Clara, CA, September 21-22, 1999, pp.132-139.
5. W. W. Van Arsdell and S. B. Brown, “Subcritical Crack Growth in Silicon MEMS,” *Journal of Microelectromechanical Systems, vol. 8, no. 3, Sept. 1999,* pp. 319-327.
6. Freeman, D.M., Aranyosi, A.J., Gordon, M.J., and Hong, S.S., “Multidimensional motion analysis of MEMS using computer microvision,” in *Tech. Dig., Solid-State Sensor and Actuator Workshop*, Hilton Head Is., SC; June 8-11, 1998, pp. 150-155.
7. D.J. Burns and H.F. Helbig, "A System for Automatic Electrical and Optical Characterization of Microelectromechanical Devices", *Journal of Microelectromechanical Systems, vol. 8, no. 4, Dec. 1999*, pp. 473-482.
8. LabVIEW, National Instruments Corporation, 11500 N Mopac Expressway, Austin, TX 78759-3504.